PAPER • OPEN ACCESS

Low-cost vertical taper for highly efficient light in-coupling in bimodal nanointerferometric waveguide biosensors

To cite this article: Daniel Grajales *et al* 2019 *J. Phys. Photonics* **1** 025002

View the article online for updates and enhancements.

JPhys Photonics

PAPER

Low-cost vertical taper for highly efficient light in-coupling in bimodal nanointerferometric waveguide biosensors

Daniel Grajales[1], Adrián Fernández Gavela[1], Carlos Domínguez[2] , Jose Ramón Sendra[3] and Laura M Lechuga[1]

1 Nanobiosensors and Bioanalytical Applications Group, Catalan Institute of Nanoscience and Nanotechnology (ICN2), CSIC, BIST and CIBER-BBN, Campus UAB, 08193, Barcelona, Spain
2 Instituto de Microelectrónica de Barcelona (IMB-CNM, CSIC), Campus UAB, 08193, Barcelona, Spain
3 IUMA, Institute for Applied Microelectronics, University of Las Palmas GC, Campus de Tafira, E35017, Las Palmas, Gran Canaria, Spain

E-mail: Laura.Lechuga@icn2.cat

Keywords: integrated optics, biosensor, interferometer, light coupling, photonic devices
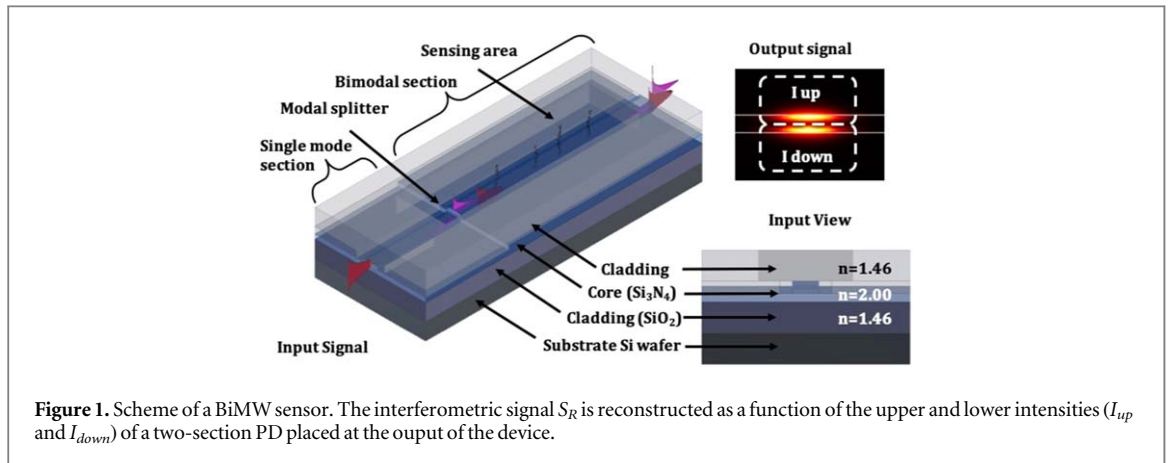
Abstract

There is still the need for a compact and cost-effective solution for efficient light in-coupling in integrated waveguides employed in photonic biosensors, especially when these waveguides are of submicron dimensions and operate at visible wavelengths. The employment of a vertically stacked taper with a larger input area is proposed to meet this need. The design of the taper is divided into two stages: in the first stage, light is guided downwards by two vertically stacked tapers; in the second stage, an inverted taper directly confines the light inside the waveguide. The design parameters are optimized using commercial software, obtaining a total theoretical light coupling efficiency of 72.25%. The taper is manufactured using SU-8 polymer as the main material, employing standard photolithography techniques at wafer level. After characterization, the results show the practicality of the taper when coupling light from macrometric sources to nanometric waveguides, obtaining an experimental coupling efficiency of 55%. With this vertical taper, a compact, easy-to-couple and cost-effective solution is achieved for waveguide-based biosensors operating at visible wavelengths, opening the way for a truly portable point-of-care biosensor for low-cost and label-free diagnostics.

1. Introduction

Portable sensor devices have become critically important as an efficient tool for environmental and clinical health diagnostics and monitoring. Photonic nanobiosensors based on evanescent wave sensing principles offer a highly sensitive and compact solution. They are shielded from electromagnetic noise and offer label-free detection for integration into portable devices. However, these sensors usually require the coupling of visible light from macrometric sources to submicron waveguides. Despite the best efforts of the photonics industry, there is no compact and cost-effective solution. Moreover, these portable biosensors must be designed to be single-use in clinical environments, making low cost and mass production key requirements.

The bimodal waveguide (BiMW) nanointerferometric biosensor presented by our group is one of the most sensitive optical biosensors for label-free detection. It is fabricated using only standard complementary metal-oxide-semiconductor technologies compatible with Si_3N_4 technology. In this device, light is coupled into a single mode waveguide section (11 800 μm long), that increases its core thickness abruptly acting as a modal splitter (from 150 nm to 340 nm thick). The modal splitter allows the propagation of only the fundamental and the first order modes. Both modes keep traveling in the bimodal section with a sensing area as cladding (15 000 μm long) followed by a bimodal section covered by SiO_2 (6750 μm long); each mode reacts differently to the same change of the refractive index in the cladding of the sensing area. After binding with bioreceptors in the surface of the sensing area, and incorporating a microfluid for sample delivery, the device could act as a highly sensitive and specific biosensor [1–3]. The scheme of the device is shown in figure 1. In order to analyze the distribution of the electromagnetic field at the output of the sensor chip, a two-section photodiode (PD) is

Figure 1. Scheme of a BiMW sensor. The interferometric signal S_R is reconstructed as a function of the upper and lower intensities (I_{up} and I_{down}) of a two-section PD placed at the ouput of the device.

located exactly at the end of the bimodal section (21 200 μm long). The intensity of the output signal will vary vertically as a function of the dephase between both modes. The interferometric signal S_R can be calculated as:

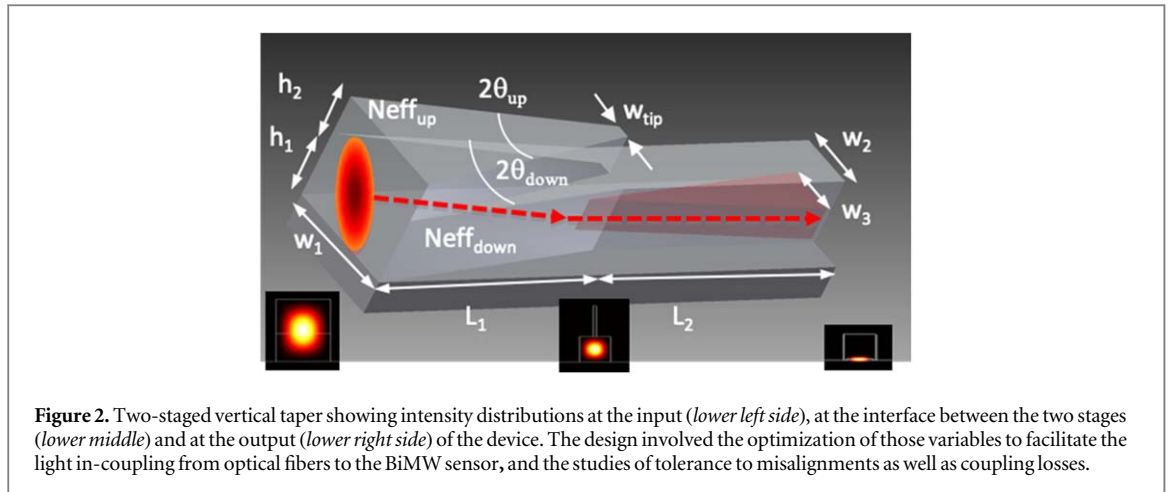$$S_R = \frac{I_{up} - I_{down}}{I_{up} + I_{down}} \tag{1}$$

where I_{up} and I_{down} are the intensities collected in the upper and lower parts of the two-section PD placed in proximity to the waveguide output, respectively. The device is capable of achieving a limit of detection (LOD) in the order of $\sim 10^{-7}$ RIU (refractive index units). This places it among the most sensitive biosensors operating under a label-free scheme [4, 5]. However, its integration into a full portable platform must surpass multiple challenges. One of them is the light in-coupling into the nanometric structures. The waveguides of the BiMW nanointerferometer must be designed at nanometric scale in order to properly guide the light at wavelengths in the visible range ($\lambda = 660$ nm) while ensuring single mode or bimodal confinement. The rib waveguide employed in the BiMW sensor, with a core of Si_3N_4 ($n_{core} = 2.00$) and cladding of SiO_2 ($n_{subs} = 1.46$), has a 3 μm $\times$ 150 nm input area [6]. With these dimensions, the efficient coupling of the light from a laser source requiring the use of macrometric elements like lenses, objectives or optical fibers is a complex step.

Current solutions for light in-coupling are mainly based on grating couplers [7]. For example, there are solutions based on subwavelength gratings [8–10], 2D arrays [11], gratings enhanced with poly-Si, metallic reflectors [12] or mirrors [13], gratings built with taper shapes [14], with conical shapes [15] or with protuberances [16], and chirped taper gratings [17]. However, due to the wavelength employed, such gratings usually require e-beam lithography or nanoimprint lithography for the fabrication of the duty cycles and etches at the nanometer scale, increasing the fabrication cost and time, and restricting integration at wafer level.

Tapers have previously been proposed for the light in-coupling due to their simple manufacture; multiple configurations and materials have been studied and fabricated, including horizontal tapers, inverted tapers [18, 19], double tip tapers [20] and silicon-on-insulator-based tapers [21] to name a few. Their disadvantages are the large length normally required to couple light and the small entrance area.

As a solution to all the above drawbacks, we propose the fabrication of a two-stage vertically stacked taper (see figure 2) as a cost-effective solution for solving the light in-coupling in a portable BiMW biosensor device. The main conditions for this taper are: (i) it must be compact while at the same time increase the coupling area to facilitate the light entry and (ii) it must be made of a material with a refractive index of between 1.46 and 2.00. Moreover, the taper should be fabricated using a material compatible with standard photolithography techniques at wafer level and with slight modification of our current BiMW fabrication process. This will preserve the low-cost requirements by facilitating the production of thousands of devices per wafer.

Although vertical tapers in SU-8 have been previously proposed in the near-IR range for applications in telecommunications, their fabrication at wafer level and integration into a photonic visible biosensor have not yet been reported [22–24]. Therefore, the design, fabrication and characterization of such an in-coupling device in the visible range are fundamental for the development of optical biosensors and for its future integration on a single chip.

Figure 2. Two-staged vertical taper showing intensity distributions at the input (*lower left side*), at the interface between the two stages (*lower middle*) and at the output (*lower right side*) of the device. The design involved the optimization of those variables to facilitate the light in-coupling from optical fibers to the BiMW sensor, and the studies of tolerance to misalignments as well as coupling losses.

2. Vertical taper design and simulation

Recapping Milton and Burst's work on tapers, we have the condition:

$$\theta < \frac{\lambda_0}{2WN_{eff}} \qquad (2)$$

where θ is the half angle of the taper (see figure 2), λ_0 is the light wavelength in the vacuum, W is the taper waist and N_{eff} the effective refractive index [25]. The smaller the angle θ, the higher the effective index N_{eff} will be, and thus more light will be guided.

Therefore, we propose a first stage made of two vertically stacked tapers with the angle of the bottom taper smaller than the angle of the upper one, $\theta_{down} < \theta_{up}$, resulting in a larger effective refractive index in the bottom section, $N_{effdown} > N_{effup}$, and thus guiding light downwards. It is required then to use a material with a refractive index value between the refractive index of the core and the refractive index of the cladding, which we will call transitional material ($n_{substrate} = n_{cladding} < n_{transitional} < n_{core}$). In the second stage, the lower waveguide has a rectangular shape incorporating a buried inverted taper which is in turn connected to the input of the BiMW itself. We choose $n_{transitional} = 1.5$ for simulations, anticipating fabrication with inexpensive materials. The proposed device and the main parameters used for the design are shown in figure 2.

2.1. Parametric design

It is necessary to use linearly polarized light as the input signal with the aim of obtaining a clear interferometric signal. During simulations, we assume that a quasi-transverse-electric (TE) polarized beam is used as the input signal. Knowing that the core diameter of a single mode, polarization-maintaining (SM-PM) optical fiber is normally 4 μm, we fix $w_1 = 5$ μm only as a starting point. For simulation purposes, we define the width-to-height ratio in a 2D analysis to ensure the light confinement of the fundamental mode across the inputs and outputs of each stage (see figure 2): $w_1/(h_1 + h_2)$ for the input of the left-hand side of stage 1; w_2/h_1 for the boundary between the right-hand side of stage 1 and the left-hand side of stage 2; and $w_3 = 3$ μm and a height of 150 nm for the right-hand side of stage 2, matching our BiMW input dimensions. Then, a width sweep was performed and total thickness values ($h_1 + h_2$) of 6 μm and 10 μm were selected, since they are feasible to fabricate by sequential deposition of 3 μm or 5 μm layers. Figure 3 shows the intensity plots of the fundamental mode in quasi-TE polarization for all the different 2D models at each of the stages. Simulations have shown that higher-order modes would be guided across the vertical taper, but it is worth remembering that the first section of the BiMW nanointerferometric biosensor is a single mode rib waveguide, and thus it acts like a mode filter: only the fundamental mode is guided to the next section. Simulations performed in FIMMPROP® (Photon Design® software) have also shown that after filtering the higher-order modes by adding a single mode waveguide of 650 μm length at the output of the vertical taper, modal coupling efficiencies of ~12% are calculated for the fundamental mode. The cut-off plots have shown that more modes will be guided as the width and height increase.

The next step is to build the 3D model for propagation and then optimize its length to keep the maximum energy confined in the shortest possible device. Table 1 shows the coupling efficiencies as a function of the length for stage 1. Even if 99% coupling efficiency could be achieved with lengths L_1 larger than 1900 μm, we want to keep the device as short as possible.
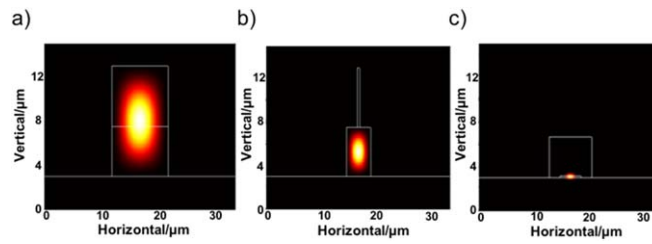
Figure 3. Intensity plots of the quasi-TE modes in 2D at the input of stage 1(a), at the output of stage 1/input of stage 2(b) and at the output of stage 2(c) of the vertical taper. Even if higher-order modes are also guided, the input of the BiMW nanointerferometric biosensor acts like a filter guiding only the fundamental mode.
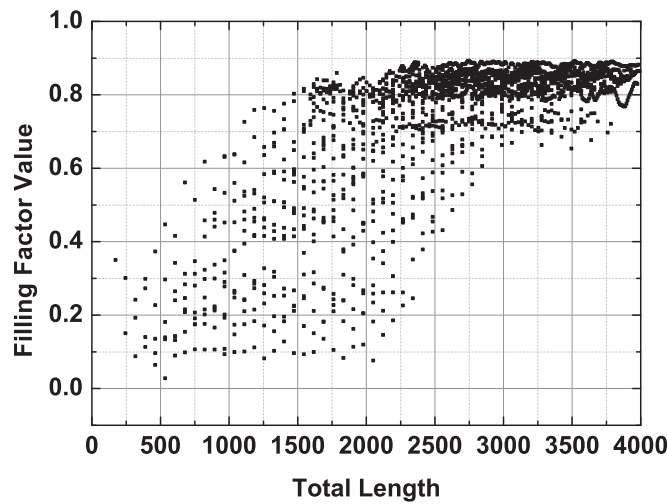

Figure 4. Filling factor value as a function of the total length (L_{tot}) of the whole taper.

Table 1. Coupling efficiency as a function of the length of stage 1 (L_1) ($h_1 = h_2 = 3$ μm and $w_1 = 10$ μm).

Length [μm]	Coupling efficiency [%]
150	76.1
250	90.3
300	94.5
500	98.3
1500	98.3
1971	99.1

Once the height and width parameters of stage 1 were defined, an optimization study of the filling factor as a function of the total length, $L_{tot} = L_1 + L_2$ was performed. The filling factor is a measure of the fraction of the mode power flux in the core guiding region as compared to the mode power flux over the whole cross-section [26, 27]. A theoretical filling factor of 100% for a given mode would mean that all the mode energy is being guided within the waveguide cross-section area. Waveguide core filling factor values of higher than 70% could be achieved with total length larger than 1200 μm, as shown in figure 4. The best trade-off between device length and transmitted energy percentage is obtained with a length of $L_1 = 330$ μm for the first stage, and $L_2 = 920$ μm for the second stage. Using these values, an efficiency of 72.25% can be obtained across the complete device (89% for stage 1 and 87% for stage 2). The final dimensions are $h_1 = h_2 = 3$ μm, $w_1 = 10$ μm, $w_2 = 6$ μm, $w_3 = 3$ μm, $L_1 = 330$ μm and $L_2 = 920$ μm, obtaining a final in-coupling area of 60 μm^2 for the vertical taper input face ($w_1 \times (h_1 + h_2)$) instead of the original coupling area of only 0.45 μm^2 (3 μm $\times$ 0.15 μm) corresponding to a single mode waveguide sensor face, without any in-coupling element. It is worth mentioning that one of the first simulation studies involved the variation of the tip width (W_{tip}) of the upper section of stage 1 between 0 and 1 μm. A higher energy confinement was observed in the case of an edged tip ($W_{tip} = 0$). However,

Figure 5. Top (a) and lateral (b) view of the proposed vertical taper (simulations were done with FIMMWAVE ® using a wavelength of 660 nm). A larger tip width of the upper taper could diminish the optical efficiency causing mode vibration as observed in the lateral view.
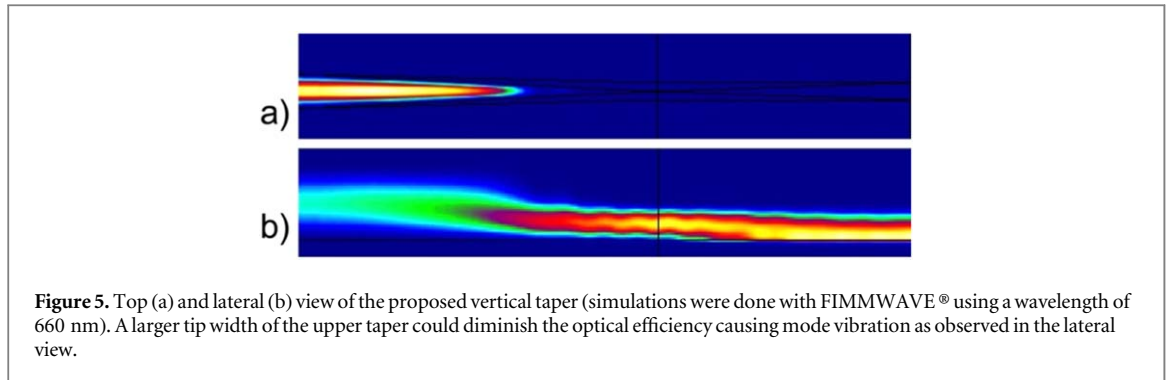
Table 2. Coupling efficiencies for different refractive indexes of possible transitional materials.

Refractive index of transitional material [RIU]	Coupling efficiency [%]
1.5	96.02
1.517	96.14
1.582	97.32
1.657	97.95
1.7	98.47
1.8	NA

due to the imperfections of the photolithographic fabrication process a tip width of some microns could be expected. Such an increase in tip width could diminish the final optical efficiency of the device and could add mode vibrations as observed in figure 5 [22]. This figure shows the simulated energy confinement for the selected dimensions.

Finally, in order to study the tolerance to refractive index variations of the intermediate material, a study was completed varying the refractive index between 1.5 and 1.8 (see table 2), concluding that indexes between 1.5 and 1.7 would work effectively.

3. Fiber in-coupling simulations

In order to simulate the effects of an optical fiber being coupled by end-fire to the input and to properly compare the taper coupling losses, all fiber optic specifications were asked of the provider (i.e. Thorlabs®) and the beam profile reconstructed and simulated in Photon Design®. Then, there are three scenarios of possible input beams: a collimated beam, a divergent beam and a convergent beam.

The first step was to simulate a collimated beam. To do so, a beam plane is located 1 μm behind the focal point. A Gaussian model with the fiber parameters previously listed was loaded. When simulating a single mode reference, x and y (horizontal and vertical, respectively) sweeps of the fiber optic position were performed and the output power plotted as a function of such misalignments. When using the vertical taper, there was a 2.9-fold increase in output power as compared with that using only the single mode waveguide.

Similarly, a convergent input beam from an optical fiber was simulated by setting a beam plane located 14.48 μm ahead of the input plane and the focal point located 1.0 μm inside the waveguide, using a Gaussian profile with horizontal polarization and a 1/ebeam width of 3.22 μm for both horizontal and vertical values. It is worth mentioning that, since it is a convergent beam, the focal point should be located a few nanometers inside the waveguide. In the case of a single mode waveguide, it is practically a butt coupling. However, the vertical taper for in-coupling does not work well in this case as we can observe the loss of one order of magnitude in the total output power. It could be the case that for butt coupling, the coupling losses are practically diminished and it is better to have a focal point inside the Si_3N_4 ($n = 2.0$) than in the SU-8 ($n = 1.59$).

Finally, in order to simulate a divergent beam incident to the input of both, a single mode reference and a vertical taper, a beam plane is located 14.48 μm ahead of the input plane and the focal point set to 14.48 μm, resulting in a divergent beam. Results from simulations have shown a two-fold increase in the total output power when using the vertical taper as compared to the single mode waveguide only.

It is worth mentioning that even if the waveguide input area is increased 133 times when using the vertical taper for in-coupling instead of the single mode waveguide, there is no direct linear relationship to the output
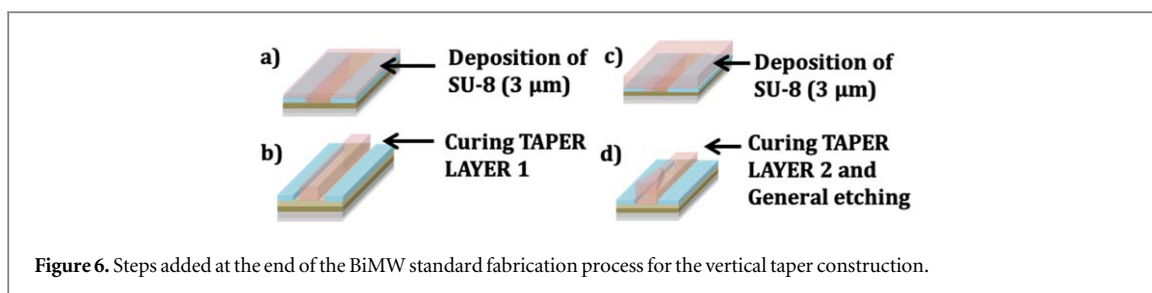
Figure 6. Steps added at the end of the BiMW standard fabrication process for the vertical taper construction.

power increase (2.9 times). However, we should remember that the increase in the input area will help to automate the in-coupling process for a compact and portable sensing platform.
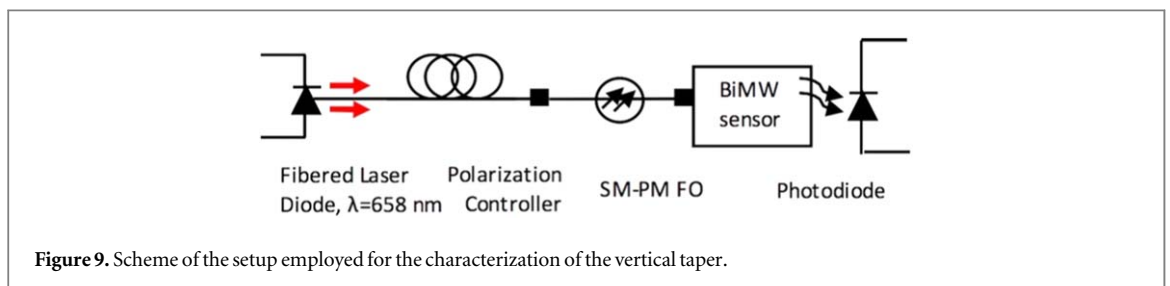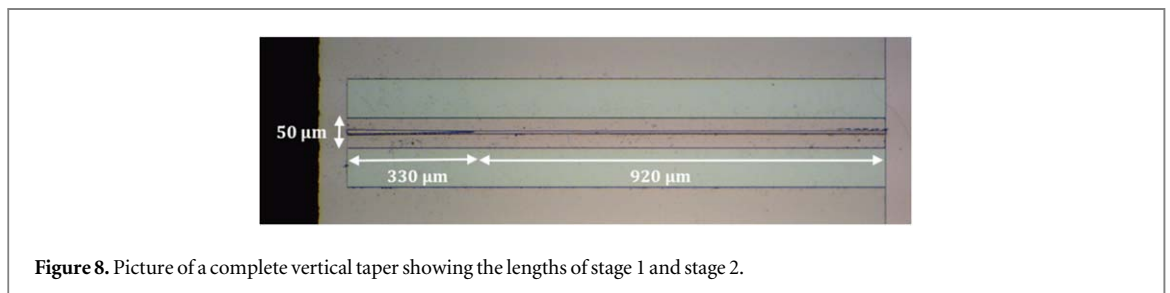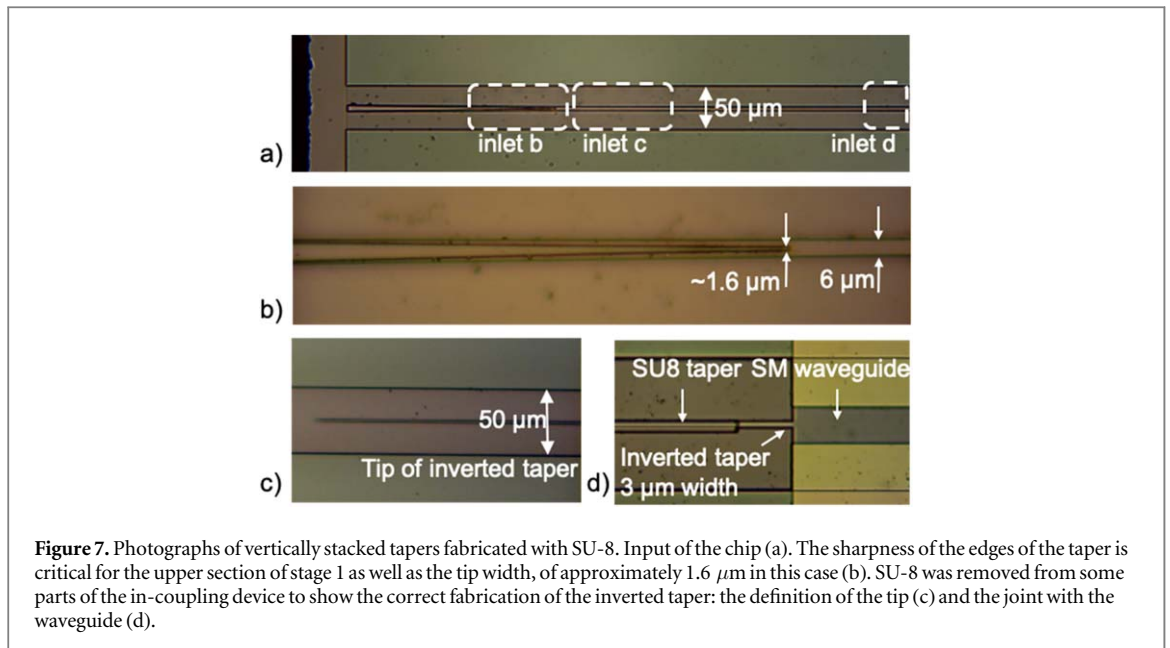
4. Vertical taper fabrication

Due to the required taper thicknesses, it could be difficult to employ Si, poly-Si, Si_3N_4 or SiO_2 structures without fracturing [28]. Such materials have a Young's modulus of between 60 GPa and 200 GPa, becoming less elastic. We therefore require a material capable of being processed at wafer level in clean room facilities, exhibiting good resistance to fracture, good bonding to SiO_2 and Si_3N_4, and with a refractive index of between 1.5 and 1.7. Moreover, the material should be processed in layers using standard lithography techniques since two levels of vertical structure are required. It should provide good resolution and definition of the structures after etching. On the other hand, we should be capable of keeping the remainder of the sensor unaffected in order to keep the sensing window of the BiMW device functional. Polymers are good candidates but it is necessary to select the right one from among the ample available options. SU-8 (SU-8 2005 permanent epoxy negative photoresist, MicroChem®) was selected for the fabrication due to its transitional refractive index and its practicability. It has a refractive index of 1.59 and resistance to elastic break and fracture (Young's modulus 2.0 GPa). SU-8 has ∼97% transmittance resulting in it being practically transparent in the visible range and particularly between 600 nm and 700 nm wavelength. It is employed at wafer level and its thickness can be controlled and cured in layers thus, after properly development, it can provide well-defined structures without affecting the rest of the sensor.

In order to compare the vertical tapers with other coupling structures such as horizontal tapers and single mode waveguide and BiMW references, lithographic masks for fabrication were designed in a modular way. Each part of the waveguide and structure was conceived as an object using GDSPy library and object-oriented programming design in Python scripts, then the GDS mask files were generated after executing the script. The design also includes, in the left side of the chip, a single mode waveguide and a BiMW to be employed as references.

4.1. Fabrication process

The taper fabrication process was implemented, including the new steps, in our well-controlled manufacturing process of BiMW sensors in our clean room facilities. Firstly, it is necessary to follow the standard fabrication of a BiMW nanointerferometric biosensor: a 2 μm SiO_2 layer is thermally grown, followed by 340 nm low pressure chemical vapor deposition of Si_3N_4. Then, the first photolithography step is applied using the first level mask to reduce the single mode section of Si_3N_4 down to 150 nm. Then a second etching process down to the Si_3N_4 layer (150 nm more) is applied using the second level mask to delineate the inverted taper, thus etching the whole Si_3N_4 layer. Next, the third level mask is used to protect and build the rib patterns across the chips defining a rib of 3.0 μm width and 2.0 nm height. Afterwards, 2 μm of SiO_2 is deposited by PECVD and the sensing regions are defined with reactive-ion etching using the fourth level of the masks. To fabricate the tapers, two extra steps were employed: deposition of 3 μm of SU-8 (spin-coated at 4500 rpm, pre-baked for 1 min at 95 °C in a hot-plate, see figure 6(a)) and curing with the fifth level mask (25 s at 365 nm wavelength, i-line, see figure 6(b)); and the immediate deposition of a second layer of 3 μm of SU-8 (spin-coated at 4500 rpm, pre-baked for 1 min at 95 °C in a hot-plate, see figure 6(c)) and curing using the sixth level of the mask set (25 s at 365 nm wavelength, i-line). Finally, both layers were developed to finalize the process and the wafer was post-baked for 2 min at 95 °C in a hot-plate (see figure 6(d)). Figure 7 shows detailed microscopic photographs of different parts of the fabricated chips. It can be observed that there is 50 μm of separation between the chip edge and the beginning of the taper in order to protect the taper during the cutting process. The SU-8 was removed from some chips in order to expose the fabricated inverted taper. The tip width of the upper section W_{tip} is calculated to be 1.6 μm approximately. Figure 8 shows a picture of a complete vertical taper.

Figure 7. Photographs of vertically stacked tapers fabricated with SU-8. Input of the chip (a). The sharpness of the edges of the taper is critical for the upper section of stage 1 as well as the tip width, of approximately 1.6 μm in this case (b). SU-8 was removed from some parts of the in-coupling device to show the correct fabrication of the inverted taper: the definition of the tip (c) and the joint with the waveguide (d).

Figure 8. Picture of a complete vertical taper showing the lengths of stage 1 and stage 2.

Figure 9. Scheme of the setup employed for the characterization of the vertical taper.

5. Vertical taper experimental evaluation

A schematic representation of the setup employed for the optical characterization of the fabricated tapers is shown in figure 9. A fibered laser diode (LD), LP660-SF60, with a peak wavelength of 658 nm and an optical power of 60 mW controlled with an ITC4005 power source through a TCLDM9 cooled mount for LDs (all of them from Thorlabs®) is employed. The single mode fiber of the LD connects to a three-paddle polarization controller (Thorlabs® FPC032), which is plugged into a commercial SM-PM optical fiber (P1-630PM-FC-2, FC/PC connectors, 630 nm, PM panda style). The ferrule from the fiber output has been fixed to the fiber holder allowing us to keep a precise control of the polarization orientation with respect to the waveguide plane. Holders and PD positioners were made in-house. Figure 10 shows a photograph of the above described setup.

For the signal read-out, a commercial two-section S4349 PD (Hamamatsu®) is connected to a PDA200 amplifier (Thorlabs®), which is in turn digitalized through an USB6361 acquisition card (National Instruments). In-house-developed object-oriented software in LabView® is used to acquire the data and process the difference in intensities between the upper (I_{up}) and the lower (I_{down}) quadrants in order to reconstruct the interferometric signal of the sensor from equation (1). A commercial power meter PM120 (Thorlabs®) is used to experimentally
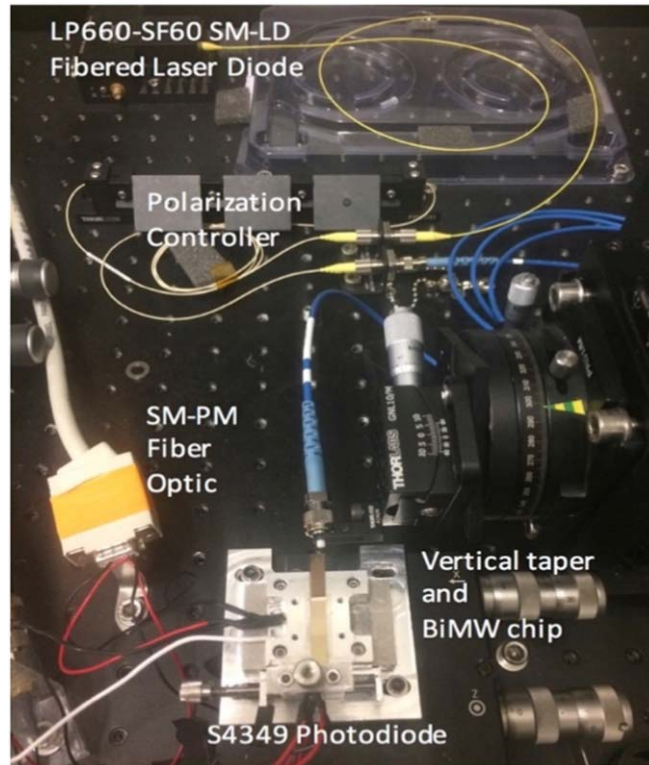
Figure 10. Photograph of the setup employed for the characterization of the vertical tapers.
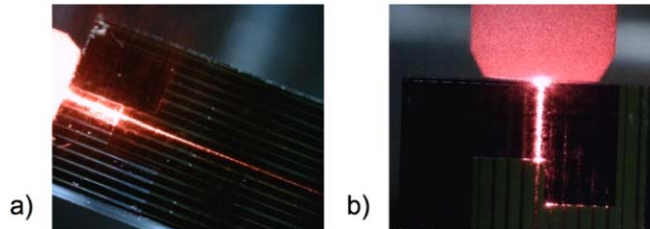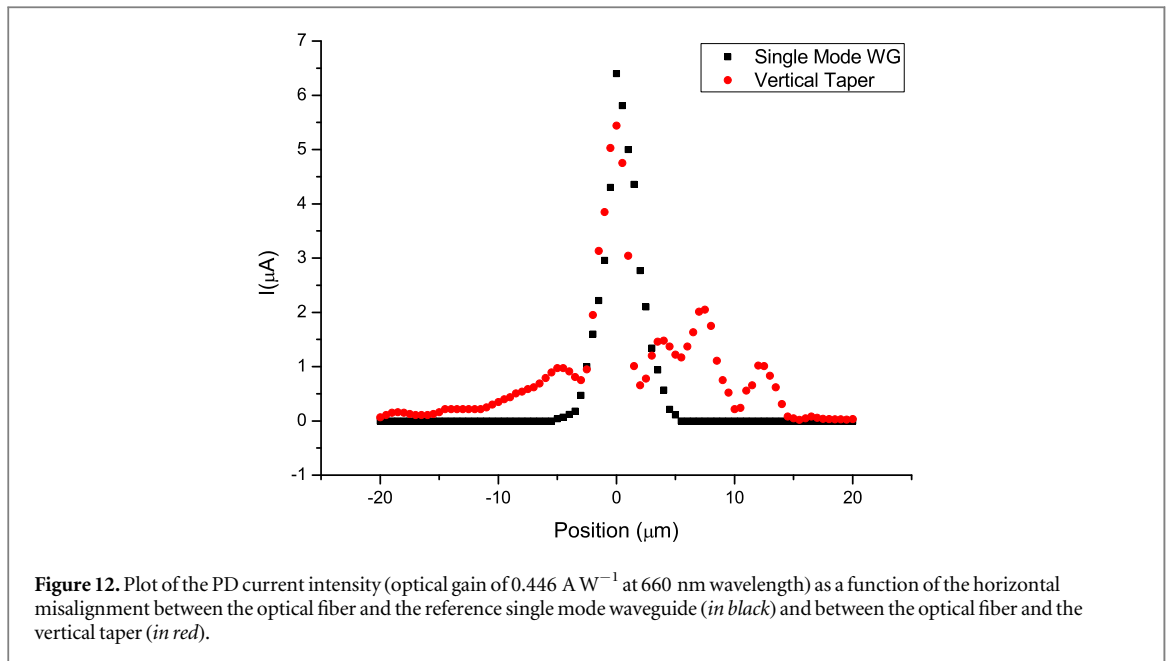

Figure 11. Lateral (a) and top (b) photographs of the light coupling in the vertical tapers from a commercial SM-PM fiber.

calculate the PD gain. Finally, an example of the direct fiber coupling with a vertically stacked taper is shown in figure 11.

5.1. Coupling losses

Knowing the experimental gain of the PD ($\sim$0.446 A W^{-1}), we have calculated the output power at the exit of the waveguides. Assuming that the total loss of power is given by $LOSS_{TOTAL}$ (dB) $= 10\text{Log}_{10}(P_{out} P_{in}^{-1}) = Coupling$ $losses + Propagation\ losses + PD\ coupling\ losses$, one could disregard the coupling losses of the read-out because their value remains the same across experiments (the PD was the same), and the propagation losses because the length of the device is constant. Thus, the total loss as read at the output would be approximately equal to the coupling loss.

By comparing the difference in output power of the reference single mode waveguide (input power in quasi-TE polarization $P_{inTE} = 1.13$ mW, output power in quasi-TE polarization $P_{outTE} = 0.246\ \mu$W, coupling loss $= 36.62$ dB) and the vertical taper with single mode waveguide ($P_{inTE} = 1.13$ mW, $P_{outTE} = 0.134\ \mu$W, coupling loss $= 39.25$ dB), we have obtained an additional coupling loss of 2.63 dB (55%) for the taper, which is not far from our theoretical calculation of 1.42 dB (72%) performed at the end of section 2.1. Due to fabrication limitations, the taper structures are not perfectly flat, and roughness could play an important role in scattering. Scattering is obvious across the taper as seen in figure 11(a); such scattering losses could explain part of the power loss. Additionally, as showed in figure 11(b), there is a percentage of scattering at the interface between the

Figure 12. Plot of the PD current intensity (optical gain of 0.446 A W^{-1} at 660 nm wavelength) as a function of the horizontal misalignment between the optical fiber and the reference single mode waveguide (*in black*) and between the optical fiber and the vertical taper (*in red*).

vertical taper and the single mode waveguide. Perhaps light is being radiated or reflected when passing from the SU-8 rectangular waveguide at the last part of stage 2 of the vertical taper to the SiO$_2$ and Si$_3$N$_4$ waveguide.

5.2. Coupling tolerance to misalignments

It is remarkable that thanks to the increase in the in-coupling area, the light coupling using a commercial optical fiber was done in a much simpler and faster way as compared to coupling by end-fire. A sweep in the horizontal alignment was performed to experimentally quantify the improvement. The fiber was positioned in the vertical taper in-coupling area where the maximum output power was obtained. From there, 1 μm steps were taken in each direction while recording the intensity reported by the PD current. A similar experiment was performed using a reference single mode waveguide directly coupled by the light from a fiber. It is worth mentioning that, since it is an interferometric signal calculated as relative to the total intensity, it would be possible to perform interferometric detections as long as the signal is 3 dB above the noise level.
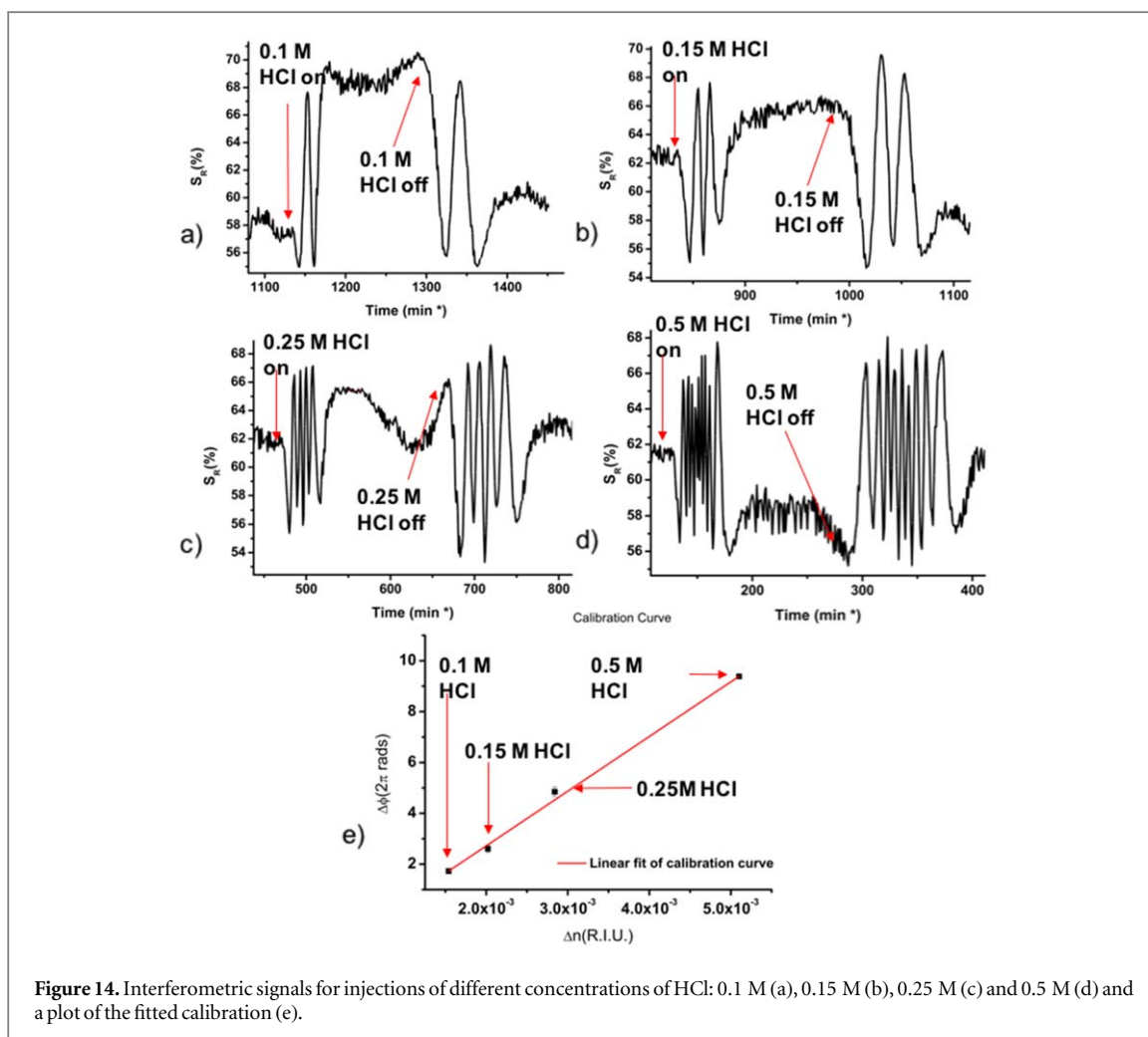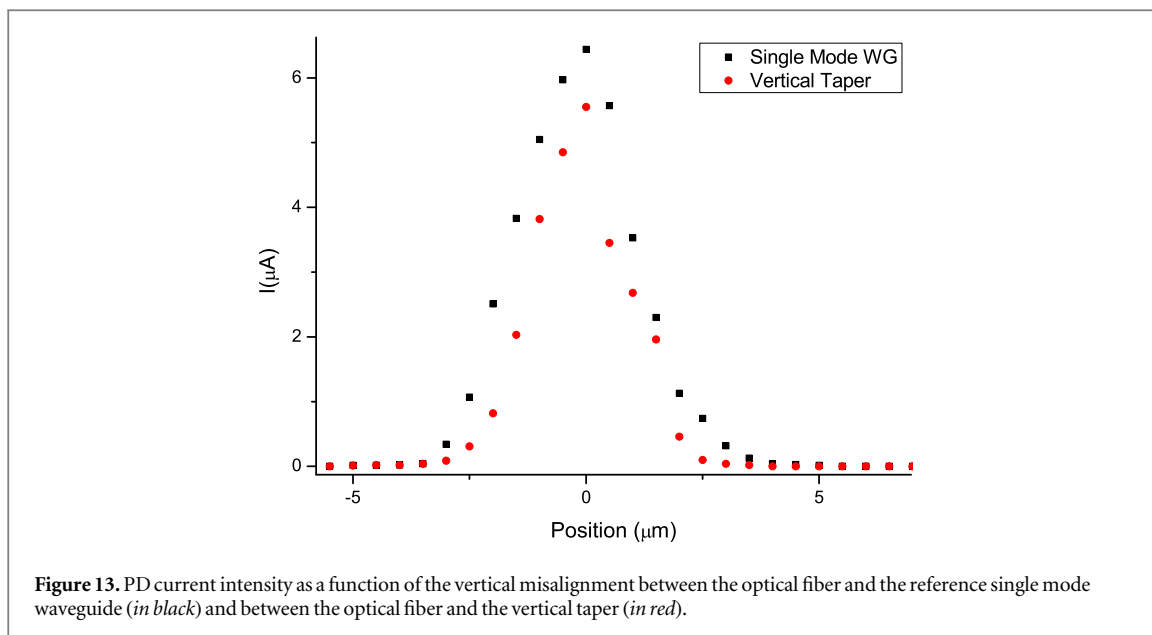
We define the acceptance waist as the range of tolerance to misalignments in which there is still sufficient intensity to perform an interferometric detection (i.e. 3 dB above the noise level). Figure 12 shows an acceptance waist of 8 μm when coupling to the reference single mode waveguide by end-fire (black dots, i.e. without vertical taper). Meanwhile, the vertical taper has an acceptance waist of 38 μm, as shown by the red plot in figure 12, when using the same end-fire method. This represents an increase of 4.75 times in coupling tolerance to misalignments in the horizontal axis. With these alignment tolerances, it would be possible to automate the in-coupling mechanisms in order to use disposable sensor cartridges in a portable platform. A static fiber source with polarized light could focus the light to the input of the vertical taper on the sensor chips which in turn could be correctly positioned through alignment marks between the disposable cartridge and the mechanical holder.

On the other hand, there is no reported improvement in terms of total output power or tolerance to vertical misalignments, as observed in figure 13. In this case, a vertical sweep with steps of 1 μm was performed experimentally and the PD current intensity recorded and plotted. Both curves have similar waists and peaks ($\sim$3 μm). As shown in the previous simulations, the advantages of the vertical taper could apply when using collimated or divergent beams as in our case.

5.3. Sensor calibration

As a proof of concept of the performance of the vertical taper approach, we have done a refractive index calibration of the BiMW sensor device. This type of calibration is normally employed for evanescent wave sensors to gain an initial insight into their sensitivity performance in bulk. In the case of the BiMW sensors with standard end-fire coupling, we have previously reported a LOD of 2 $\times$ 10^{-7} RIU by using this refractive index calibration approach. A calibration curve was obtained injecting four different concentrations of HCl (0.5 M, 0.25 M, 0.15 M and 0.1 M at 30 μl min^{-1}), which correspond to minute variations of the refractive index over the sensing window (see figure 14 and table 3).

Computing and plotting the phase shift corresponding to each refractive index difference will provide us with the calibration plot. The slope of this plot corresponds to the bulk sensitivity S_{bulk} intrinsic to the sensor,

Figure 13. PD current intensity as a function of the vertical misalignment between the optical fiber and the reference single mode waveguide (*in black*) and between the optical fiber and the vertical taper (*in red*).

Figure 14. Interferometric signals for injections of different concentrations of HCl: 0.1 M (a), 0.15 M (b), 0.25 M (c) and 0.5 M (d) and a plot of the fitted calibration (e).

which is $2150 \cdot 2\pi$ rad RIU^{-1}. A LOD of 2.98×10^{-6} RIU is calculated for a system baseline noise of 0.1282% and visibility of 15%. There is a loss of one order of magnitude in the LOD when comparing the BiMW sensor coupled by end-fire to the vertical taper plus BiMW sensor. We could attribute this decrease to the presence of SU-8 debris in the sensing window which could have diminished the index contrast between the cladding and the core and, consequently, the visibility of both modes. Nevertheless, the LOD is of the same order of

Table 3 Refractive index difference from deionized H_2O ($nH_2O = 1.3332$) to different dilutions of HCl and the corresponding phase shift.

HCl concentration [Molar]	Refractive index difference [RIU]	Phase shift [2π rad]
0.5	0.051	9.38
0.25	0.002 84	4.84
0.15	0.002 02	2.60
0.1	0.001 54	1.72

magnitude as that reported in most state-of-the-art evanescent wave sensors. On the other hand, the possibility of using commercial SM-PM fiber optics to couple directly to the BiMW biosensor opens the possibility of automation and further point-of-care integration of BiMW technology.

6. Conclusions

A low-cost taper solution made out of SU-8 polymer for coupling visible light into nanometric Si_3N_4 photonic waveguides has been designed, simulated, fabricated and tested. Via simulations, it was foreseen that the vertical taper solution would be effective when coupling collimated or divergent beams. Besides, a 4.75-fold increase in the horizontal tolerance to misalignment has been proved, paving the way for automated coupling mechanisms. Moreover, SU-8 has been employed for fabrication at wafer level allowing mass production, low cost and fast fabrication, by employing standard microelectronics technology and adding only three extra photolithographic mask levels to the current fabrication process of the BiMW. As a proof of concept, a calibration curve was calculated showing a bulk sensitivity of $2150 \cdot 2\pi$ rad RIU^{-1} and a LOD of 2.98×10^{-6} RIU, which are very competitive values as compared to the state-of-the-art in evanescent wave sensing. This way, larger macrometric light sources could be more easily in-coupled, paving the way towards an automated in-coupling mechanism for portable biosensor analyzers.

Acknowledgments

ORCID iDs

Carlos Domínguez ⓘ https://orcid.org/0000-0002-5972-7285
Laura M Lechuga ⓘ https://orcid.org/0000-0001-5187-5358

References

[1] Huertas C S, Fariña D and Lechuga L M 2016 *ACS Sensors* **1** 748–56
[2] Maldonado J, González-Guerrero A B, Domínguez C and Lechuga L M 2016 *Biosens. Bioelectron.* **85** 310–6
[3] González-Guerrero A B, Maldonado J, Dante S, Grajales D and Lechuga L M 2017 *J. Biophoton.* **10** 61–7
[4] Estevez M C, Alvarez M and Lechuga L M 2012 *Laser Photon. Rev.* **6** 463–87
[5] Fernández Gavela A, Grajales García D, Ramirez J C and Lechuga L M 2016 *Sensors* **16** 285
[6] Zinoviev K E, González-Guerrero A B, Domínguez C and Lechuga L M 2011 *J. Light. Technol.* **29** 1926–30
[7] Vermeulen D, Selvaraja S, Verheyen P, Lepage G, Bogaerts W, Absil P, Van Thourhout D and Roelkens G 2010 *Opt. Express* **18** 18278–83
[8] Cheben P, Xu D-X, Janz S and Densmore A 2006 *Opt. Express* **14** 4695–702
[9] Flueckiger J, Schmidt S, Donzella V, Sherwali A, Ratner D M, Chrostowski L and Cheung K C 2016 *Opt. Express* **24** 15672–86
[10] Zhu L, Yang W and Chang-Hasnain C 2017 *Opt. Express* **25** 18462–73
[11] Taillaert D, Chong H, Borel P I, Frandsen L H, De La Rue R M and Baets R 2003 *IEEE Photonics Technol. Lett.* **15** 1249–51
[12] Romero-García S, Merget F, Zhong F, Finkelstein H and Witzens J 2013 *Opt. Lett.* **38** 2521–3
[13] Orobtchouk R, Layadi A, Gualous H, Pascal D, Koster A and Laval S 2000 *Appl. Opt.* **39** 5773–7
[14] Markov P, Valentine J G and Weiss S M 2012 *Opt. Express* **20** 14705–13
[15] Ropers C, Neacsu C C, Elsaesser T, Albrecht M, Raschke M B and Lienau C 2007 *Nano Lett.* **7** 2784–8

[16] Chen B *et al* 2016 *Nanoscale* **8** 12189–201

[17] Triggs G J, Wang Y, Reardon C P, Fischer M, Evans G J O and Krauss T F 2017 *Optica* **4** 229–34

[18] Porte H, Ben Bakir B and Bernabe S 2011 *8th IEEE Int. Conf. on Group IV Photonics* (London: The Royal Society) pp 386–8

[19] Pu M, Liu L, Ou H, Yvind K and Hvam J M 2010 *Opt. Commun.* **283** 3678–82

[20] Tao S H, Song J, Fang Q, Yu M B, Lo G Q and Kwong D L 2008 *Opt. Express* **16** 20803–8

[21] Roelkens G, Dumon P, Bogaerts W, Van Thourhout D and Baets R 2005 *IEEE Photonics Technol. Lett.* **17** 2613–5

[22] Pan Z, Subbaraman H, Zou Y, Xu X, Zhang X, Zhang C, Li Q, Jay Guo L and Chen R T 2015 *Photonics Res.* **3** 317–23

[23] Fu Y, Ye T, Tang W and Chu T 2014 *Photonics Res.* **2** A41–4

[24] Khilo A, Popović M A, Araghchini M and Kärtner F X 2010 *Opt. Express* **18** 15790–806

[25] Milton A and Burns W 1977 *IEEE J. Quantum Electron.* **13** 828–35

[26] Photon Design 2009 FIMMWAVE manual Version 5.2 © 1997–2009

[27] Daldosso N, Melchiorri M, Riboli F, Girardini M, Pucker G, Crivellari M, Bellutti P, Lui A and Pavesi L 2004 *J. Light. Technol.* **22** 1734–40

[28] Suwito W, Dunn M L, Cunningham S J and Read D T 1999 *J. Appl. Phys.* **85** 3519–34